

Three-dimensional sensing of the magnetic-field vector by a compact planar-type Hall device

Junichi Shiogai ¹✉, Kohei Fujiwara ¹, Tsutomu Nojima ¹ & Atsushi Tsukazaki ^{1,2,3}

Smart society is forthcoming with a rapid development in the automation of electric appliances requiring abundant sensors. One of the key sensors is a three-dimensional magnetometer for detecting the motion of objects, which is usually driven by cooperative multiple sensors on three orthogonal planes. Here, we demonstrate the fundamental operation of a three-dimensional magnetometer based on a simple Fe-Sn heterostructure Hall device in a planar geometry. Polar coordinates of the magnetic-field vector are uniquely determined by the combination of the sizable anomalous Hall effect, the anisotropic magnetoresistance, and the unidirectional magnetoresistance. Thanks to the ferromagnetic topological features in the Fe-Sn heterostructure, the above-mentioned device overcomes the limitation of conventional semiconductor devices and is highly sensitive even at room temperature. The compact planar geometry will be particularly useful in versatile electrical applications requiring a low-cost three-dimensional magnetometer with space- and energy-saving features.

¹Institute for Materials Research, Tohoku University, 2-1-1 Katahira, Aoba-Ku, Sendai 980-8577, Japan. ²Center for Spintronics Research Network (CSRN), Tohoku University, 2-1-1 Katahira, Aoba-Ku, Sendai 980-8577, Japan. ³Center for Science and Innovation in Spintronics (CSIS), Tohoku University, 2-1-1 Katahira, Aoba-Ku, Sendai 980-8577, Japan. ✉email: junichi.shiogai@tohoku.ac.jp

As demand for magnetic-field sensing increases in a recently developing internet-of-things (IoT) society, the various types of magnetometers have been developed and immensely contributed to a broad range of applications^{1–4}. The most commonly used two types of magnetometers are semiconductor Hall sensors^{5,6} and ferromagnetic magnetoresistive sensors^{7,8}, which generate the output signal against the scalar quantity of the magnetic field along a principal axis. However, future automation in the automotive industry and robotics requires detecting the motion of objects via determination of the magnetic field (\mathbf{H}) vector in three dimensions, enabling the control of precise position, angle, and rotation of fundamental components in an electric appliance. For magnetic-field sensing in three dimensions, individual detection of the three-dimensional (3D) components of the magnetic field is necessary. The classical way to detect 3D components of \mathbf{H} includes placing three Hall sensors^{5,9–11} or magnetoresistive sensors orthogonally (along x -, y -, and z -axis)^{12–14} and attaching magnetic flux guides in the planar devices^{15,16}. However, these techniques face the requirements of three power sources and 3D space arrangement. To expand the 3D sensing of the magnetic field into versatile electric appliances, it is essential to develop the 3D magnetometer based on a single planar-type device with low power consumption and a simple measurement unit. The appealing phenomena in ferromagnetic films such as spin-orbit torque¹⁷ and unidirectional magnetoresistance (UMR)¹⁸ are beneficial to trigger the development of a planar 3D magnetometer beyond the conventional Hall devices.

The 3D sensing of the magnetic-field vector corresponds to the function for the detection of the magnetic field amplitude and direction with polar coordinates. Figure 1a represents the magnetic-field vector \mathbf{H} with its amplitude H , polar angle θ_H , and azimuthal angle ϕ_H . The 3D magnetometer has to uniquely determine these polar coordinates via electrical measurements. Typically, the Hall effect is available to measure the amplitude H

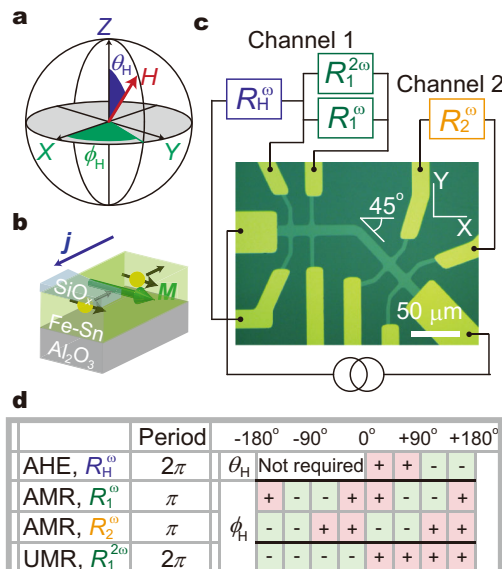


Fig. 1 Detection concept for magnetic-field vector by a Fe-Sn heterostructure device. **a** Definition of the polar (θ_H) and azimuthal (ϕ_H) angles of the magnetic-field vector \mathbf{H} . **b** Schematic of layer structure consisting of a SiO_x cap and 4-nm-thick Fe-Sn layer grown on Al_2O_3 substrate. Magnetization of the Fe-Sn layer follows the magnetic field, providing resistance changes with respect to strength and direction of the field. **c** Top-view photograph of the planar Hall device and measurement setup. **d** Summary of the signal output from AHE, AMR, and UMR.

and the polar angle θ_H . Conventional semiconductors, such as Si, GaAs, and InAs, have been well applied to practical Hall magnetometers owing to good controllability of sensitivity based on high-mobility charge carriers⁵. Recently, in addition to the conventional semiconductor devices driven by the ordinary Hall effect, ferromagnetic heterostructures with high Curie temperatures have been recognized as a good candidate for the room-temperature Hall magnetometer^{19–21}, driven by anomalous Hall effect (AHE)²². In particular, the sizable anomalous Hall response for the detection of H is enabled by the intrinsic mechanism owing to the specific band features of the topologically nontrivial ferromagnetic materials^{22,23}. Moreover, the determination of azimuthal angle ϕ_H is critically important to develop compact planar-type 3D magnetometers since it is rather difficult for a single semiconductor Hall device. By using magnetic materials, anisotropic magnetoresistance (AMR) is applicable to measure the ϕ_H because its amplitude reflects the relative angle between in-plane directions of electric current (\mathbf{I}) and magnetization (\mathbf{M})⁷. When the direction of \mathbf{M} follows to \mathbf{H} , the AMR provides the information of the direction of \mathbf{H} . However, the AMR in one component provides four identical values owing to the 180° period, which is insufficient to uniquely determine the ϕ_H .

In this study, we apply two AMR probes and UMR effect^{18,24–28} to solve this problem. Here, we report on the demonstration of magnetic-field vector detection by implementing the AHE, AMR, and UMR effects into a single planar-type 3D magnetometer based on the ferromagnetic Fe-Sn heterostructure. The device overcomes the limitation of conventional semiconductor devices and is highly sensitive at room temperature.

Results and discussion

Concept of device structure and measurement setup. A SiO_x capped 4-nm-thick Fe-Sn heterostructure (Fig. 1b) was patterned into a device consisting of two Hall-bar channels oriented along x -axis (channel 1) and -45° from x -axis (channel 2) in series, as shown in Fig. 1c. To disentangle the AMR and UMR signals, harmonics measurements of the sheet and Hall resistance were employed using lock-in amplifiers under the application of the ac current with modulation frequency $f = 2\pi\omega$ ²⁴. The first harmonic Hall resistance R_H^ω and the first and second harmonic sheet resistance R_1^ω and R_2^ω for channel 1, and the first harmonic sheet resistance R_2^ω for channel 2 were measured simultaneously. Figure 1d summarizes the concept for the determination of the polar coordinates θ_H by R_H^ω and ϕ_H by R_1^ω , R_2^ω , and $R_1^{2\omega}$. The polar angle θ_H (out-of-plane field direction) is monitored by R_H^ω via AHE. In usual polar coordinates, the θ_H should be only defined in $0^\circ \leq \theta_H \leq 180^\circ$. The azimuthal angle ϕ_H (in-plane field direction) is measured by the values of R_1^ω and R_2^ω and the sign of UMR in $R_1^{2\omega}$. Judging from the combination of two AMR values R_1^ω and R_2^ω , four identical values are reduced to two. The UMR signal follows the sign of $\mathbf{M} \times \mathbf{I}$ under broken inversion symmetry along out-of-plane direction¹⁸, resulting in a 360° period against ϕ_H . As a consequence, the combinations of positive and negative values of θ_H and ϕ_H listed in Fig. 1d resolve the unique direction of a magnetic-field vector by simultaneous measurements of AHE, AMR, and UMR in the ferromagnetic heterostructure device.

Vector rotation in xz plane for verification of θ_H detection. The AHE was evaluated to examine the correspondence between the R_H^ω and the \mathbf{H} direction as shown in Fig. 2. Under the perpendicular \mathbf{H} condition in Fig. 2a, the R_H^ω increases linearly up to $\mu_0 H = 0.6$ T with no hysteresis behavior, being suitable for detection of out-of-plane component of the magnetic field. The measurable amplitude of H is limited to the saturation field of M , which can be modulated by the magnetic shape anisotropy or the

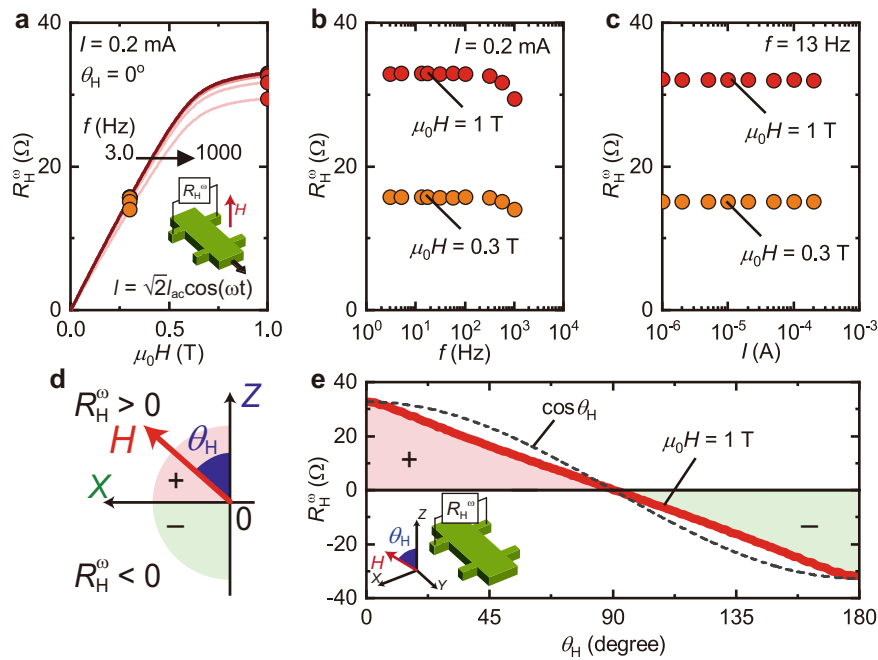


Fig. 2 Hall effect measurements for determination of θ_H . **a** Hall resistance (R_H^ω) as a function of out-of-plane magnetic field ($\mu_0 H$) measured at 0.2 mA with various modulation frequency from 3 Hz to 1 kHz. The data below $f = 300$ Hz are merged in a single curve. **b, c** The values of R_H^ω at $\mu_0 H = 0.3$ and 1 T plotted as a function of the modulation frequency f (**b**) and amplitude of current (**c**). **d** Schematic of θ_H rotation of the magnetic field (H). R_H^ω produces a positive value for $0 < \theta_H < 90^\circ$ (red region) while it produces a negative value for $90^\circ < \theta_H < 180^\circ$ (green). **e** θ_H dependence of R_H^ω when $\mu_0 H = 1$ T. The H was rotated in the xz plane (inset).

interfacial magnetic anisotropy. The extracted values of R_H^ω at $\mu_0 H = 0.3$ and 1 T are plotted as a function of modulation frequency f (Fig. 2b) and current amplitude I_{ac} (Fig. 2c). The Hall resistance R_H^ω is stably maintained against f and I_{ac} , meaning that the Ohmic behavior persists in high frequency up to 300 Hz. The large Hall voltage under ac operation is an essential prerequisite for sensor application in terms of detectivity²⁹ and low-energy consumption⁵. Figure 2d, e represent the polar angle θ_H dependence of R_H^ω measured at 1 T. The R_H^ω is initially positive when $\mu_0 H = 1$ T points along $+z$ ($\theta_H = 0^\circ$). With sweeping θ_H from 0° to 180° in the xz plane, the R_H^ω monotonically decreases with sign reversal at $\theta_H = 90^\circ$. Note that the $R_H^\omega(\theta_H)$ did not follow the sinusoidal function of θ_H (black dashed line), implying that the magnetization was not saturated along the direction of $\mu_0 H = 1$ T due to the in-plane magnetic anisotropy (Supplementary Note 3 and Supplementary Fig. 3). While the amplitude of H should be evaluated from two values of different component R_1^ω and R_2^ω (Supplementary Note 4), the normalized function of $R_H^\omega(\theta_H)$ guarantees that the angle of θ_H is uniquely determined in the range of $0^\circ \leq \theta_H \leq 180^\circ$. Note that $R_H^\omega(\theta_H)$ can be a good reference curve for identifying θ_H even if the magnetization is not saturated along H .

Vector rotation in xy plane for verification of ϕ_H detection. We here refer to the determination of the azimuthal angle ϕ_H using AMR and UMR in the magnetic Fe–Sn Hall-bar device. The primary and secondary harmonic components of R_1^ω , R_2^ω , and $R_1^{2\omega}$ as shown in Fig. 3a were measured during magnetic-field rotation in the xy plane. By contrast to the well-studied 180° period of AMR⁷, the UMR signal expectedly exhibits 360° period as depicted in Fig. 3b^{24,25}. Figure 3c presents typical AMR, the variations of R_1^ω and R_2^ω (denoted as ΔR_1^ω and ΔR_2^ω) as a function of ϕ_H under $\mu_0 H = 1$ T. The periodic functions of ΔR_1^ω and ΔR_2^ω with 180° indicate that the resistance variation becomes positively

large when the field is parallel to the current whereas it is negatively large when the field is perpendicular to the current. The AMR signal obeys sinusoidal function of $\cos^2 \phi_H$ (black dashed lines), implying that the direction of in-plane M follows that of H . This agreement can be ascribed to the isotropic feature of M in the sample plane. The AMR amplitude R_1^{AMR} and R_2^{AMR} , defined by a half value of the peak-to-peak amplitude of $\Delta R_1^\omega(\phi_H)$ and $\Delta R_2^\omega(\phi_H)$ (vertical black arrows in Fig. 3c) corresponds to about 0.1% of the base resistance of about 800 Ω , which is a typical value of ferromagnetic metals³⁰. The phase shift $\Delta \phi_H$ between ΔR_1^ω and ΔR_2^ω defined in Fig. 3c and AMR signal amplitude are plotted in Fig. 3d as a function of ac injection current I_{ac} . The uniform distribution of electric current along the series channel 1 and 2 is maintained in the three orders of magnitude in I_{ac} . With the almost constant phase shift of $45.2 \pm 0.75^\circ$, the simultaneous measurement of R_1^ω and R_2^ω allows the two possible angles of ϕ_H in either $0 < \phi_H < 180^\circ$ or $-180 < \phi_H < 0^\circ$. To uniquely determine ϕ_H in the range of $-180^\circ < \phi_H < 180^\circ$, the UMR plays a significant role although a signal amplitude at room temperature is rather small compared to that of AMR.

Figure 3e shows the UMR of $R_1^{2\omega}$ measured with I_{ac} of 0.2 mA, which is 360° period with its sign being positive in $0^\circ < \phi_H < 180^\circ$ and negative for $-180^\circ < \phi_H < 0^\circ$ (see also Supplementary Note 7 and Supplementary Fig. 6). This valid judgment enables us to define ϕ_H uniquely. The amplitude of UMR signal characterized by $R_1^{\text{UMR}} = [\Delta R_1^{2\omega}(\phi_H = 90^\circ) - \Delta R_1^{2\omega}(\phi_H = -90^\circ)]/2$ in Fig. 3f linearly increases with increasing the amplitude I_{ac} , which is consistent to the origin of UMR effect at the broken inversion symmetry at the interface with Rashba spin-orbit interaction¹⁸ or magnetothermal effect^{25,31}. The relative amplitude of UMR to the channel resistance per current density $\frac{R_1^{\text{UMR}}/R_1^\omega}{I_{ac}/tw} = 4.14 \times 10^{-16}$ ($\text{m}^2 \text{A}^{-1}$) with $R_1^{\text{UMR}}/I_{ac} = 8.42 \Omega \text{A}^{-1}$ being a linear slope in Fig. 3f, $t = 4$ nm Fe–Sn film thickness, $w = 10 \mu\text{m}$ the channel width, and the $R_1^\omega = 813 \Omega$. This value is five times larger than the reported value

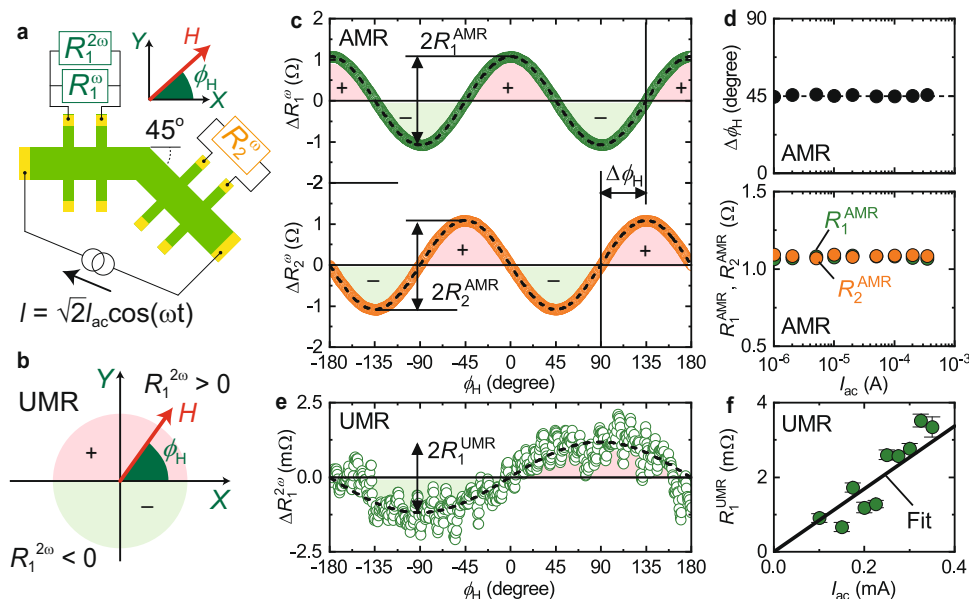


Fig. 3 AMR and UMR measurements for determination of θ_H . **a** Top view of measurement setup. **b** Schematic of ϕ_H rotation of the magnetic field. The UMR signal measured in $R_1^{2\omega}$ produces a positive value for $0^\circ < \phi_H < 180^\circ$ (red region) while it produces a negative value for $-180^\circ < \phi_H < 0^\circ$ (green). **c** ϕ_H dependences of ΔR_1^ω (green circles) and ΔR_2^ω (orange circles) when $\mu_0 H = 1$ T was rotated in the xy plane. The measurement was performed at $I_{ac} = 0.2$ mA and $f = 13$ Hz. **d** Current amplitude (I_{ac}) dependence of the phase shift of ϕ_H ($\Delta\phi_H$) between the AMR signals, defined by the horizontal arrow in **(c)**, and AMR signal R_1^{AMR} (green circles) and R_2^{AMR} (orange circles), defined by the vertical arrows in **(c)**. **e** ϕ_H dependence of $\Delta R_1^{2\omega}$ when $\mu_0 H = 1$ T was rotated in the xy plane. **f** I_{ac} dependence of UMR signal R_1^{UMR} defined as vertical arrows in **(e)**. Error bars denote the interval with the 95% reliability.

in heavy metal/ferromagnet bilayer heterostructures²⁵ (Supplementary Note 5 and Supplementary Table 2). In the trilayer structure of $\text{SiO}_x/4\text{-nm-thick Fe-Sn}/\text{Al}_2\text{O}_3$ substrate, the band offsets at the top and bottom interfaces may not be perfectly canceled, leading to the broken inversion symmetry along the out-of-plane direction. The amplitude of UMR may be further enhanced by optimizing the layer structure³¹ or by introducing a superlattice structure. Considering the large AHE of the Fe–Sn nanocrystalline thin films fabricated by sputtering technique, which is probably ascribed to the intrinsic mechanism^{21,32}, the spin-orbit interaction and specific band feature cooperatively contributes to yield the large UMR effect at room temperature. Combining the AMR originated from \mathbf{M} and the UMR from broken inversion symmetry and specific band structure, the ϕ_H is uniquely determined in a planar-type Hall device based on ferromagnetic Fe–Sn heterostructure.

Experimental demonstration of 3D magnetic-field sensing.

Finally, we demonstrated the detection of the magnetic-field vector consisting of θ_H and ϕ_H with a constant magnetic-field strength of 1 T along the flow chart depicted in Fig. 4a. The determination of θ_H and ϕ_H was performed by the evaluation of R_H^ω using AHE, and R_1^ω and R_2^ω using AMR and UMR, subsequently. Here, $R_H^\omega(\theta_H)$ at $\mu_0 H = 1$ T (Fig. 2e) was used for the determination of θ_H . The beforehand determination of θ_H is a reasonable route to explore the magnetic-field direction since the Hall effect is a simple and independent measurement. Following the determination of θ_H , the AMR curve defines two possible in-plane directions ϕ_H or $\phi_H - 180^\circ$. Note that because the amplitude of AMR depends on θ_H , the comparison with the normalized reference curves (Supplementary Note 6 and Supplementary Fig. 5) is necessary. Then, the sign of UMR in $R_1^{2\omega}$ is employed to uniquely determine ϕ_H . The reference curves of $R_H^\omega(\theta_H)$, $R_1^\omega(\phi_H)$, and $R_2^\omega(\phi_H)$ depend on the scalar quantity of the magnetic field \mathbf{H} . Therefore, for determination of ϕ_H and θ_H , the scalar quantity of \mathbf{H} should be first evaluated by the independent analysis of R_1^ω and R_2^ω (Supplementary Note 4 and Supplementary Fig. 4) and the

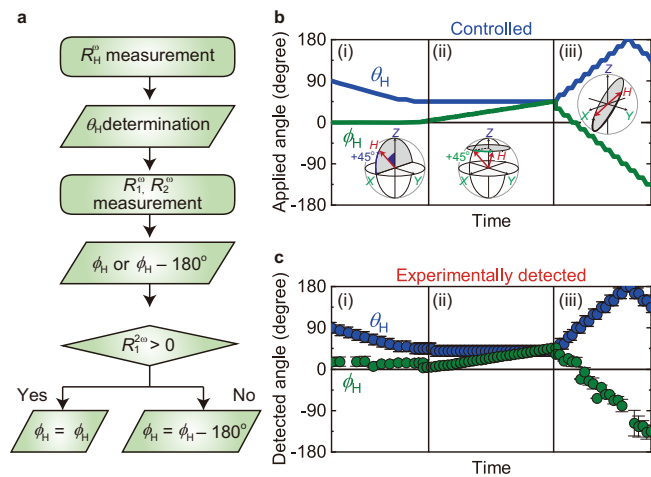


Fig. 4 Demonstration of detection of the magnetic field vector. **a** Flow chart for determination of the magnetic-field vector by the Fe–Sn magnetometer. The polar angle θ_H is determined by R_H^ω through AHE whereas the azimuthal angle ϕ_H is determined by R_1^ω , R_2^ω , and the sign of $R_1^{2\omega}$ through AMR and UMR, respectively. **b** Time evolution of θ_H (blue) and ϕ_H (green) of the controlled magnetic field \mathbf{H} . Schematics for the rotation of \mathbf{H} vector is depicted in insets. **c** Experimentally detected θ_H and ϕ_H by the Fe–Sn device. The error bar of θ_H and ϕ_H was defined by the contribution of AMR to R_H^ω and the difference in detected angles by R_1^ω and R_2^ω , respectively.

cross-checking of the projected value of \mathbf{H} along z -direction with θ_H . As demonstration for the determination of magnetic-field vector \mathbf{H} , the intentionally controlled \mathbf{H} shown in Fig. 4b was measured with a planar Fe–Sn Hall device in a superconducting vector magnet. In the regions (i)–(iii), the sensing operation was examined along the out-of-plane rotation, in-plane rotation, and diagonal rotation. Figure 4c shows the time evolution of the experimentally detected θ_H and ϕ_H . The θ_H rotation (blue) at xz

plane in the region (i) is systematically detected by R_H^ω , which is consistent to controlled θ_H from 90° to 45° . Then, the ϕ_H rotation (green) under $\theta_H = 45^\circ$ in the region (ii) is evaluated by the AMR curves of R_1^ω and R_2^ω and the sign of UMR in $R_1^{2\omega}$. For the diagonal rotation examination, the subsequent scan of θ_H and ϕ_H was performed in the region (iii). At each step of θ_H rotation, the flow chart of Fig. 4a was applied to determine the angles. Overall, the excellent agreement between controlled and experimentally detected magnetic-field angles demonstrates that the planar-type single Fe–Sn device is capable of detecting the magnetic-field vector in three dimensions. Although the present demonstration was performed at $\mu_0 H = 1$ T, the flow chart of Fig. 4a is valid by selecting the proper reference curve of $R_H^\omega(\theta_H)$, $R_1^\omega(\phi_H)$, and $R_2^\omega(\phi_H)$ depending on the field strength (Supplementary Note 4). Along this detection process, the device is capable of detecting the magnetic-field vector in the range of 0.1–1.0 T with a sensitivity of $0.4 \text{ V A}^{-1} \text{ degree}^{-1}$ for θ_H , $0.04 \text{ V A}^{-1} \text{ degree}^{-1}$ for ϕ_H and $51.3 \text{ V A}^{-1} \text{ T}^{-1}$ for the field amplitude (see Supplementary Note 8 and Supplementary Table 3). The detection functionality may be further extended by evaluating the scalar quantity of the field (Supplementary Fig. 4), such as detecting the position of the moving object.

Conclusion

By employing AHE, AMR, and UMR, we have demonstrated a feasible detection of the magnetic field vector with a Fe–Sn heterostructure-based Hall device. Compared with conventional semiconductor Hall sensors and magnetoresistance sensors, the advantages of our device are a compact device in a planar geometry with a single current source and a room-temperature fabrication process with abundant non-toxic elements. The simple configuration of the 3D magnetometer enables us to expand the possibility of implementing the various conventional sensors in smart electronics. The aspect of the low-cost sputtering process of the Fe–Sn-based magnetometers is an advantage in integration into the conventional silicon-based circuits or flexible substrate. The observation of the substantial signal from UMR in a $\text{SiO}_2/\text{Fe–Sn}/\text{Al}_2\text{O}_3$ structure implies the importance of a specific band structure with the spin–orbit interaction at the heterointerface. The device performance will be further improved by applying extensive knowledge of topological material science owing to large AHE and specific UMR effect originating from the electronic band topology and spin–orbit interaction^{22,32–34}.

Methods

Sample preparation. The heterostructure consisting of 4-nm-thick $\text{Fe}_{0.62}\text{Sn}_{0.38}$ ferromagnetic layer and SiO_x cap layer was grown by co-sputtering technique at room temperature on $\text{Al}_2\text{O}_3(0001)$ single crystal substrate. The thickness was measured by X-ray reflectivity (Supplementary Note 1 and Supplementary Fig. 1). The Fe/Sn composition ratio was calibrated using electron energy dispersive X-ray spectroscopy in a 48-nm-thick film deposited at the identical condition with the 4-nm-thick sample. We examined the uniformity of the Fe composition in as wide as a few mm^2 in the film (Supplementary Note 1 and Supplementary Table 1). The device was fabricated with the $\text{SiO}_2/\text{Fe–Sn}/\text{Al}_2\text{O}_3$ heterostructure by photolithography and Ar ion milling. The Ti/Pt electrodes were defined by photolithography and deposited by ion beam sputtering at room temperature after in situ Ar ion milling.

Electrical measurements. The device was placed in a variable temperature insert equipped with a superconducting vector magnet. Details of the measurement setup are shown in Supplementary Note 2 and Supplementary Figure 2. The measurement was performed by a lock-in technique at 300 K. The primary component of the channel resistance and Hall resistance were measured at the same frequency 13 Hz of the current by lock-in amplifiers. The secondary harmonic component of the resistance was measured by a lock-in amplifier with a second harmonic mode.

Data availability

Data supporting the findings of this study are available from the corresponding author upon reasonable request.

Received: 8 April 2021; Accepted: 9 September 2021;

Published online: 04 October 2021

References

- Lenz, J. E. A review of magnetic sensors. *Proc. IEEE* **78**, 973–989 (1990).
- Heremans, J. Solid state magnetic field sensors and applications. *J. Phys. D: Appl. Phys.* **26**, 1149–1168 (1993).
- Lenz, J. & Edelstein, A. S. Magnetic sensors and their applications. *IEEE Sens. J.* **6**, 631–649 (2006).
- Michelena, M. D. Small magnetic sensors for space applications. *Sensors (Basel)* **9**, 2271–2288 (2009).
- Popović, R. S. *Hall Effect Devices*. (Institute of Physics Publishing, Bristol and Philadelphia, 2004).
- Boero, G., Demierre, M., Besse, P. A. & Popovic, R. S. Micro-Hall devices: performance, technologies and applications. *Sens. Actuators A* **106**, 314–320 (2003).
- Mapps, D. J. Magnetoresistive sensors. *Sens. Actuators A* **59**, 9–19 (1997).
- Zheng, C. et al. Magnetoresistive sensor development roadmap (Non-Recording Applications). *IEEE Trans. Magn.* **55**, 0800130 (2019).
- Popovic, R. S. The vertical Hall-effect device. *IEEE Electron Device Lett* **5**, 357–358 (1984).
- Kordic, S. & Munter, P. J. A. Three-dimensional magnetic-field sensors. *IEEE Electron Device Lett* **35**, 771–779 (1988).
- Schott, C., Racz, R., Manco, A. & Simonne, N. CMOS single-chip electronic compass with microcontroller. *IEEE J. Solid State Circuits* **42**, 2923–2933 (2007).
- Ettelt, D. et al. 3D magnetic field sensor concept for use in inertial measurement units (IMUs). *J. Microelectromech. Syst.* **23**, 324–333 (2014).
- Trinh, X. T. et al. Miniature tri-axis magnetometer with in-plane GMR sensors. *IEEE Trans. Magn.* **53**, 4004304 (2017).
- Becker, C. et al. Self-assembly of highly sensitive 3D magnetic field vector angular encoders. *Sci. Adv.* **5**, eaay7459 (2019).
- Luong, V. S. et al. Planarization, fabrication and characterization of three-dimensional magnetic field sensors. *IEEE Trans. Nanotechnol.* **17**, 11–25 (2017).
- Chen, J., Wurz, M. C., Belski, A. & Rissing, L. Designs and characterizations of soft magnetic flux guides in a 3-D magnetic field sensor. *IEEE Trans. Magn.* **48**, 1481–1484 (2012).
- Li, R. et al. A spin–orbit torque device for sensing three-dimensional magnetic fields. *Nat. Electron.* **4**, 179–184 (2021).
- Tokura, Y. & Nagaosa, N. Nonreciprocal responses from noncentrosymmetric quantum materials. *Nat. Commun.* **9**, 3740 (2018).
- Chen, Y. J., Basiaga, D., O'Brien, J. R. & Heiman, D. Anomalous magnetic properties and Hall effect in ferromagnetic Co_2MnAl epilayers. *Appl. Phys. Lett.* **84**, 4301 (2004).
- Vilanova Vidal, E., Stryanyuk, G., Schneider, H., Felser, C. & Jakob, G. Exploring Co_2MnAl Heusler compound for anomalous Hall effect sensors. *Appl. Phys. Lett.* **99**, 132509 (2011).
- Satake, Y., Fujiwara, K., Shiojari, J., Seki, T. & Tsukazaki, A. Fe–Sn nanocrystalline films for flexible magnetic sensors with high thermal stability. *Sci. Rep.* **9**, 3282 (2019).
- Nagaosa, N., Sinova, J., Onoda, S., MacDonald, A. H. & Ong, N. P. Anomalous Hall effect. *Rev. Mod. Phys.* **82**, 1539–1592 (2010).
- Karplus, R. & Luttinger, J. M. Hall effect in ferromagnetics. *Phys. Rev.* **95**, 1154–1160 (1954).
- Avcı, C. O. et al. Unidirectional spin Hall magnetoresistance in ferromagnet/normal metal bilayers. *Nat. Phys.* **11**, 570–575 (2015).
- Avcı, C. O. et al. Magnetoresistance of heavy and light metal/ferromagnet bilayers. *Appl. Phys. Lett.* **107**, 192405 (2015).
- Olejník, K., Novák, V., Wunderlich, J. & Jungwirth, T. Electrical detection of magnetization reversal without auxiliary magnets. *Phys. Rev. B* **91**, 180402(R) (2015).
- Yasuda, K. et al. Large unidirectional magnetoresistance in a magnetic topological insulator. *Phys. Rev. Lett.* **117**, 127202 (2016).
- Lv, Y. et al. Unidirectional spin–Hall and Rashba–Edelstein magnetoresistance in topological insulator–ferromagnet layer heterostructures. *Nat. Commun.* **9**, 111 (2018).
- Shiojari, J., Jin, Z., Satake, Y., Fujiwara, K. & Tsukazaki, A. Low-frequency noise measurements on Fe–Sn Hall sensors. *Appl. Phys. Express* **12**, 123001 (2019).
- Kokado, S., Tsunoda, M., Harigaya, K. & Sakuma, A. Anisotropic magnetoresistance effects in Fe, Co, Ni, Fe_3N , and half-metallic ferromagnet: a systematic analysis. *J. Phys. Soc. Jpn.* **81**, 024705 (2012).
- Lidig, C. et al. Unidirectional Spin Hall magnetoresistance as a tool for probing the interfacial spin polarization of Co_2MnSi . *Phys. Rev. Appl.* **11**, 044039 (2019).
- Fujiwara, K. et al. Doping-induced enhancement of anomalous Hall coefficient in Fe–Sn nanocrystalline films for highly sensitive Hall sensors. *APL Mater.* **7**, 111103 (2019).

33. Ye, L. et al. Massive Dirac fermions in a ferromagnetic kagome metal. *Nature* **555**, 638–642 (2018).
34. Nagaosa, N., Morimoto, T. & Tokura, Y. Transport, magnetic and optical properties of Weyl materials. *Nat. Rev. Mater.* **5**, 621–636 (2020).

Acknowledgements

This work was partly supported by CREST (No. JPMJCR18T2). Device fabrication was performed in the Cooperative Research and Development Center for Advanced Materials under the GIMRT Program of the Institute for Materials Research, Tohoku University (Proposal No. 20G0407). We thank NEOARK Corporation for the use of photo-lithography equipment for device fabrication.

Author contributions

J.S. and A.T. conceived the project. J.S. performed device fabrication and electrical transport measurements with the help of T.N. K.F. fabricated the thin film samples. J.S. and A.T. wrote the paper. All authors discussed the results.

Competing interests

The authors declare no competing interests.

Additional information

Supplementary information The online version contains supplementary material available at <https://doi.org/10.1038/s43246-021-00206-2>.

Correspondence and requests for materials should be addressed to Junichi Shioyai.

Peer review information *Communications Materials* thanks Long You and the other, anonymous, reviewer(s) for their contribution to the peer review of this work. Primary Handling Editors: Aldo Isidori. Peer reviewer reports are available.

Reprints and permission information is available at <http://www.nature.com/reprints>

Publisher's note Springer Nature remains neutral with regard to jurisdictional claims in published maps and institutional affiliations.



Open Access This article is licensed under a Creative Commons Attribution 4.0 International License, which permits use, sharing, adaptation, distribution and reproduction in any medium or format, as long as you give appropriate credit to the original author(s) and the source, provide a link to the Creative Commons license, and indicate if changes were made. The images or other third party material in this article are included in the article's Creative Commons license, unless indicated otherwise in a credit line to the material. If material is not included in the article's Creative Commons license and your intended use is not permitted by statutory regulation or exceeds the permitted use, you will need to obtain permission directly from the copyright holder. To view a copy of this license, visit <http://creativecommons.org/licenses/by/4.0/>.

© The Author(s) 2021